IEEE Photonics Journal
An IEEE Photonics Society Publication

Open Access

Multiband Switchable Terahertz Quarter-Wave Plates via Phase-Change Metasurfaces

Volume 8, Number 1, February 2016

Dacheng Wang
Lingchao Zhang
Yandong Gong
Linke Jian
T. Venkatesan
Cheng-Wei Qiu
Minghui Hong

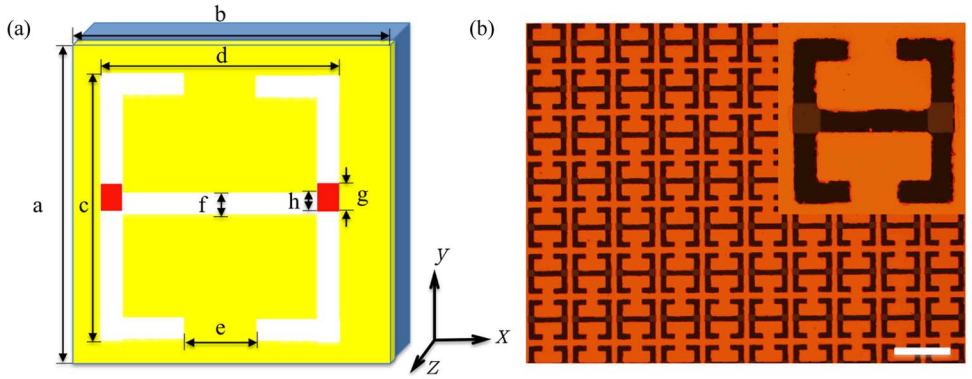

DOI: 10.1109/JPHOT.2016.2514717
1943-0655

Multiband Switchable Terahertz Quarter-Wave Plates via Phase-Change Metasurfaces

Dacheng Wang,[1,2] Lingchao Zhang,[3,4] Yandong Gong,[2] Linke Jian,[4] T. Venkatesan,[1,3,4,5] Cheng-Wei Qiu,[1] and Minghui Hong[1]

[1]Department of Electrical and Computer Engineering, National University of Singapore, Singapore 117576
[2]Institute for Infocomm Research, Singapore 138632
[3]Department of Physics, National University of Singapore, Singapore 117542
[4]NUSNNI-NanoCore, National University of Singapore, Singapore 117411
[5]Materials Science and Engineering and Integrative Science and Engineering, National University of Singapore, Singapore 117456

DOI: 10.1109/JPHOT.2016.2514717

Manuscript received November 30, 2015; revised December 26, 2015; accepted January 4, 2016. Date of publication January 5, 2016; date of current version January 26, 2016. This work was supported in part by the National Research Foundation, Prime Minister's Office, Singapore, under its Competitive Research Program (CRP Awards NRF-CRP10-2012-04 and NRF-CRP4-2008-04) and in part by SERC A*STAR, Singapore, under Project 1420200044. Corresponding author: M. Hong (e-mail: elehmh@nus.edu.sg).

Abstract: Metasurfaces open up a low-dimensional artificial approach to tailor electromagnetic (EM) waves with unprecedented functionalities. However, the ability to actively control and manipulate EM waves via metasurfaces still faces challenges that need to be overcome. Here, we experimentally demonstrated a multiband switchable terahertz quarter-wave plate via inserting a phase-change material, i.e., vanadium dioxide (VO_2), into complementary electric split-ring resonators. Before the VO_2 phase transition, this phase-change metasurface achieves linear-to-circular polarization conversion at 0.45 and 1.10 THz with an ellipticity of 0.998 and -0.971, respectively. After the VO_2 phase transition, linear-to-circular polarization conversion is obtained at both 0.50 and 1.05 THz with an ellipticity of 0.999 and -0.999, respectively. This work reveals the feasibility of using phase-change metasurfaces for multiband tunable active terahertz polarization control, and such compact tunable devices can be designed for other frequency regimes as well.

Index Terms: Metasurfaces, terahertz optics, phase-change materials, quarter-wave plate.

1. Introduction

Metasurfaces have attracted intense research interest because they offer exceptional potential for shaping the wavefront of electromagnetic (EM) waves beyond that which can be obtained by natural materials. Composed of low-dimensional artificial resonators, metasurfaces provide significant flexibility to control the amplitude, phase, and propagation of EM waves by changing the geometry, size, orientation, and material of the resonators [1]–[8]. The thickness of resonators is on a sub-wavelength scale, which can be applied to flat optics design, such as flat lens, wave plates and holograms [9]–[12]. Meanwhile, gradient metasurfaces have been used to demonstrate unconventional light bending [13], [14], vortex beam generation [15], and coding

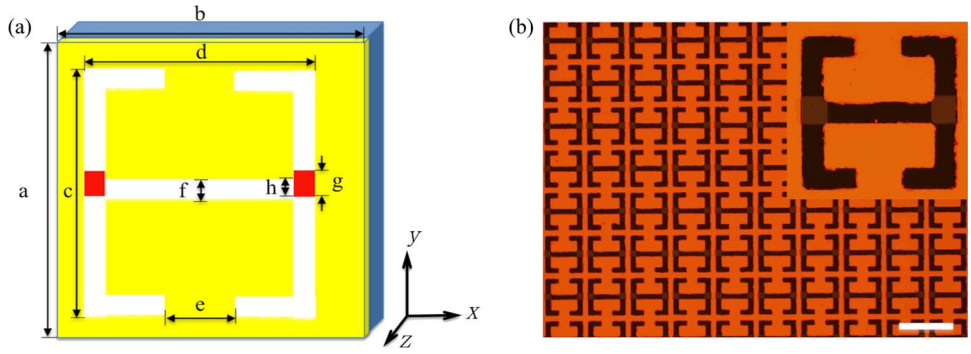

Fig. 1. (a) Schematic view of the unit cell in the designed phase-change metasurfaces. The geometrical parameters are the following: a = b = 80, c = d = 70, e = 26, f = g = 9, and h = 8 μm. (b) Optical microscope image of the fabricated phase-change metasurfaces with an enlarged image of the unit cell at the top right. The scale bar is 100 μm.

holograms [16]. The propagation directions of EM waves illuminating the gradient metasurfaces can be described by the generalized laws of refraction and reflection. These fascinating properties make metasurfaces a significant platform for planar photonics. However, most metasurfaces lack the flexibility to dynamically control the EM responses. The development of active metasurfaces would further create an extremely fertile ground for their applications.

Recently active metasurfaces have been investigated by hybridizing the resonators with various active media, such as semiconductor, phase-change material, graphene, liquid crystal and biased diode [17]–[24]. These active metasurfaces present exotic optical activities in deflected beam modulation [18], handedness switching [25], polarization conversion [19], anomalous refraction [20], and multifunctional photonic switching [21]. In particular, active manipulation of the polarization states via metasurfaces in the terahertz (THz) region presents new opportunities for terahertz optics in polarimetric imaging, circular dichroism characterization and signal transmission. One of the advantages of THz active metasurfaces is that the inserted active media can extend the operating frequencies of the meta-devices. For instance, our previous work demonstrated a switchable THz quarter-wave plate at two operating frequencies [19]. To further extend the operating frequencies, in this work, we experimentally demonstrate a multiband switchable THz quarter-wave plate. This active meta-device consists of complementary electric split-ring resonators (C-ESRRs) embedded with vanadium dioxide (VO_2), a phase change material. Before the VO_2 phase transition, the quarter wave-plate presents two operating frequencies with high polarization conversion. After the VO_2 phase transition, both operating frequencies can be switched to two other frequencies retaining the high polarization conversion. This multiband operating frequency switching is attributed to the variation of the effective length of resonators and the damping effect introduced by VO_2. Such multiband active metasurfaces open up a new avenue for low-dimensional tunable meta-devices.

2. Design, Fabrication, and Characterization

The multiband switchable THz quarter-wave plate was designed using commercial software CST Microwave studio. The schematic view of the designed phase-change metasurface is shown in Fig. 1(a). It consists of copper C-ESRRs (yellow part) and VO_2 pads (red part) on a sapphire substrate. The periodicity of the unit cell is a = b = 80 μm. The lengths of C-ESRRs along *x*- and *y*-axes are c = d = 70 μm. The gap size and line width of C-ESRRs are e = 26 μm and f = 9 μm, respectively. The length of VO_2 pads is g = 9 μm and the width of VO_2 pads is the same as the line width of C-ESRRs. The gap size between the upper side of C-ESRRs and the bottom side of VO_2 is h = 8 μm, as shown in Fig. 1(a). In the simulation, the sapphire substrate was treated as a lossless dielectric (dielectric constant $\varepsilon_{sub} = 11.5$), and the copper film was modeled as a lossy metal (conductivity $\sigma = 5.8 \times 10^7$ S/m). The optical properties of VO_2 were

simulated using Drude Model, which was described in our previous work [19]. Before the phase transition at 300 K, the electrical conductivity of VO_2 was modeled as $\sigma = 140$ S/m. After the phase transition at 400 K, the electrical conductivity of VO_2 was simulated as $\sigma = 5 \times 10^5$ S/m. The complex transmission $\tilde{t}_{sim\_x}$ and $\tilde{t}_{sim\_y}$ were obtained when the incident polarization was along *x*- and *y*-axes, respectively [24]. To make the phase-change metasurface function as a quarter-wave plate, the geometrical parameters were optimized to meet the following criteria: $|\tilde{t}_{sim\_x}| = |\tilde{t}_{sim\_y}|$ and $|\arg(\tilde{t}_{sim\_x}) - \arg(\tilde{t}_{sim\_y})| = 90°$. Meanwhile, our previous work demonstrated that in such phase-change metasurface based quarter-wave plate design, the numerical designed phase delay should be larger than 90° to experimentally obtain a perfect polarization conversion. Thus, we optimized the phase delay to be larger than 90°.

The phase-change metasurfaces were fabricated by photolithography. Firstly, a 200 nm thick M phase VO_2 film was grown on a c-cut sapphire substrate by pulsed laser deposition. Then a layer of photoresist was spin coated on the VO_2 film. The VO_2 pads were defined on the photoresist by photolithography. Ion milling was used to etch away the VO_2 area that was not protected by the photoresist. The next step was to hybridize the copper C-ESRRs with the VO_2 pads. A layer of photoresist was spin coated on the sample followed by UV exposure in the photolithography system with proper alignment. After the photoresist development, a 200 nm thick copper film with a 10 nm thick adhesion layer of chromium was deposited on the sample by a thermal evaporator (Edwards Auto 306). A lift-off process was carried out to form the designed phase-change metasurfaces. The optical microscope image of the fabricated sample is shown in Fig. 1(b). The overall size of the sample is 1×1 cm^2.

The sample was measured using the terahertz time-domain spectroscopy (THz-TDS) [19], [27]. In this characterization system, GaAs-based photoconductive antennas in the THz emitter and detector were pumped by an 800 nm wavelength femtosecond laser with a pulse duration of 12 fs and repetition rate of 80 MHz. The input and output polarization states of the THz wave were controlled by two wire-grid polarizers placed in front of the emitter and detector. The incident electric field was polarized at $\theta = 45°$ to *x*-axis. The transmitted electric fields along *x*- and *y*-axes were recorded as $\overline{E}_x$ and $\overline{E}_y$. The reference electric fields $\overline{E}_x(ref)$ and $\overline{E}_y(ref)$ were measured using a bare sapphire substrate. The normalized transmission spectra were obtained as $|\tilde{t}_x| = |\overline{E}_x/\overline{E}_x(ref)|$ and $|\tilde{t}_y| = |\overline{E}_y/\overline{E}_y(ref)|$. The phase delay of the electric fields between *y*- and *x*-axes was calculated by fast Fourier transform, which was noted as $\varphi = \varphi_y - \varphi_x = \arg(\tilde{t}_y) - \arg(\tilde{t}_x)$. During the characterization, the VO_2 phase transition was controlled by a resistive heater with a square aperture $(6 \times 6$ mm$^2)$ milled at the center. An infrared camera (FLIR Systems i60) was employed to monitor the temperature of the sample in real time to ensure the VO_2 phase transition.

3. Results and Discussion

The measured transmission spectra and phase delays of this phase-change metasurface at 300 K are shown in Fig. 2(a) and (b). It is observed that before the VO_2 phase transition at 300 K, the phase-change metasurface functions as a THz quarter-wave plate at two operating frequencies. At 0.45 THz, the transmission coefficients along the *x*- and *y*-axes are 0.564 and 0.573, respectively. The phase delay between the *y*- and *x*-axes is 93.5°. At 1.10 THz, the transmission coefficients along the *x*- and *y*-axes are 0.245 and 0.303, while the phase delay between the *y*- and *x*-axes is –96.5°. Therefore, at these two frequencies the output THz waves are either right-handed or left-handed circular polarized waves. The simulated transmission spectra and phase delays are shown in Fig. 2(c) and (d). As can be seen, the simulated results indicate two operating frequencies of the quarter-wave plate. A small difference can be observed in terms of the transmitted amplitude and phase delay at 0.45 THz, which attributes to size variation during the fabrication. However, the difference between experiment and simulation for the high operating frequency is more obvious. This is due to the wood's anomaly close to 1.10 THz, which can be calculated as $\lambda = P\sqrt{\varepsilon_{\text{sub}}}$, where *P* is the periodicity of the C-ESRRs,

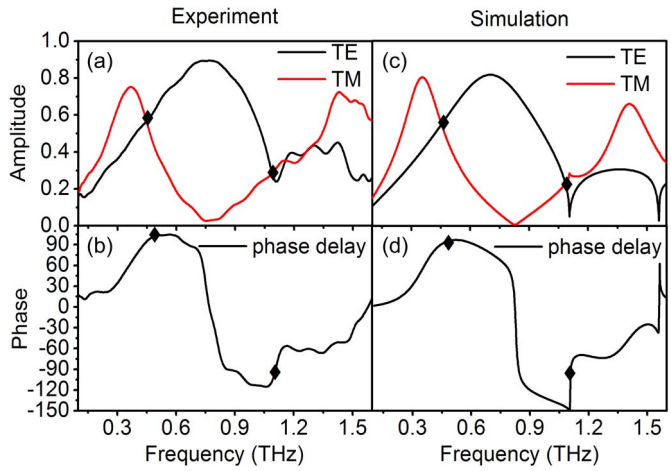

Fig. 2. (a) Measured transmission spectra of the phase-change metasurfaces before the VO_2 phase transition at 300 K and (b) the corresponding phase delay between the *y*- and *x*-axes. (c) Simulated transmission spectra of the phase-change metasurfaces with the electrical conductivity of VO_2 at $\sigma = 140$ S/m and (d) the corresponding phase delay between the *y*- and *x*-axes.

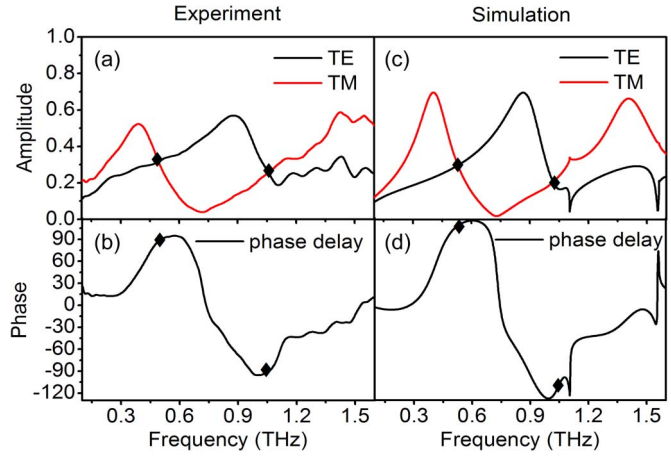

Fig. 3. (a) Measured transmission spectra of the phase-change metasurfaces after the VO_2 phase transition at 400 K and (b) the corresponding phase delay between the *y*- and *x*-axes. (c) Simulated transmission spectra of the phase-change metasurfaces with the electrical conductivity of VO_2 at $\sigma = 5 \times 10^5$ S/m and (d) the corresponding phase delay between the *y*- and *x*-axes.

and ε_{sub} is the dielectric constant of the substrate. Another reason for this difference may be attributed to loss introduced in the VO_2 pads. Despite the differences, the overall trends of the transmission spectra and phase delays between the experimental and simulation results are in good agreement. Thus, this phase-change metasurface acts as a quarter-wave plate at two operating frequencies before the VO_2 phase transition with good polarization conversion.

The performance of the quarter-wave plate after the VO_2 phase transition at 400 K is shown in Fig. 3. The measured transmission spectra and phase delays at 400 K shown in Fig. 3(a) and (b) present two operating frequencies of the quarter-wave plate. At 0.50 THz, the measured transmission coefficients along the *x*- and *y*-axes are 0.318 and 0.310, while the phase delay between the *y*- and *x*-axes is 88.9°. At 1.05 THz, the transmission coefficients along the *x*- and *y*-axes are 0.262 and 0.256. The phase difference between the *y*- and *x*-axes is -90.4°. Therefore, the quarter-wave plate shows good performance in polarization conversion in experiment. Fig. 3(c) and (d) present the simulated transmission spectra and phase delays when the electrical conductivity of VO_2 researches $\sigma = 5 \times 10^5$ S/m. From both the experimental and simulation results,

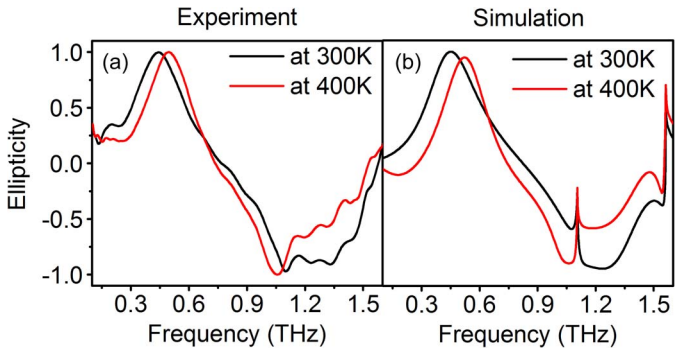

Fig. 4. (a) Measured and (b) simulated ellipticities of the transmitted terahertz wave before and after the VO_2 phase transition.

we can observe that the transmission coefficients after the VO_2 phase transition are smaller than those obtained before the VO_2 phase transition. The physics behind this discrepancy is the different losses in VO_2 pads. At 300 K, VO_2 behaves as a semiconductor and its loss is low. However, at 400 K free carriers in VO_2 increase, which leads to a high damping loss and a small transmission coefficient. In addition, the damping loss in VO_2 and the size variation during the fabrication make the transmission curve flat. Therefore, the experimental phase delay is smaller than that achieved in simulation, which is in good agreement with our previous work [19]. To obtain perfect polarization conversion, phase delay in the simulation is larger than 90°, which enables us to obtain a nearly 90° phase delay in experiment.

In order to precisely define the degree of circular polarization of the output THz wave, the Stokes parameters were calculated based on the transmission spectra and phase delays [19], [28]. When the incident THz wave linearly polarizes at θ degrees with respect to the x-axis, the electric field of the incident light can be noted as

$$\overline{E} = \overline{E}_x + \overline{E}_y = \tilde{t}_x \cos\theta + \tilde{t}_y \sin\theta. \tag{1}$$

In this phase-change metasurface, the polarization angle of the incident wave is designed to be $\theta = 45^\circ$. The Stokes parameters can be calculated using the following equations:

$$S_0 = |\overline{E}_x|^2 + |\overline{E}_y|^2 \tag{2}$$

$$S_1 = |\overline{E}_x|^2 + |\overline{E}_y|^2 \tag{3}$$

$$S_2 = 2|\overline{E}_x||\overline{E}_y| \cos\varphi \tag{4}$$

$$S_3 = 2|\overline{E}_x||\overline{E}_y| \sin\varphi. \tag{5}$$

S_0 is the total power of the output THz wave, S_1 is the difference of the output power between horizontal and vertical linearly polarized waves, S_2 is the difference of the output power between linearly polarized waves along +45° and −45°, and S_3 is the difference of the output power between right and left circular polarized waves. The polarization state of the output THz wave can be represented by ellipticity, which is defined as

$$\chi = \frac{S_3}{S_0}. \tag{6}$$

When χ equals 1, the output THz wave is a perfect left-handed circularly polarized light. When χ equals −1, the output THz wave is a perfect right-handed circularly polarized light.

Fig. 4 shows the ellipticity of the output THz wave based on the measured and simulated transmission spectra and phase delays. It is observed in Fig. 4(a) that before the VO_2 phase

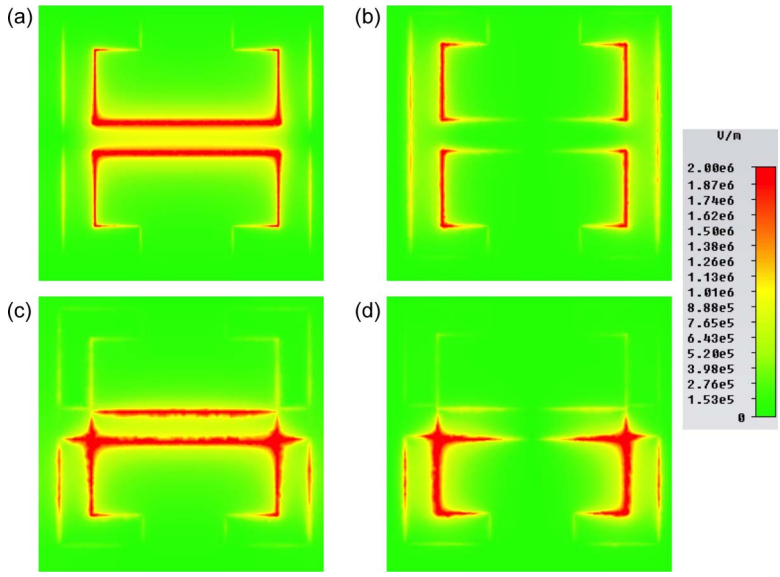

Fig. 5. Electric field distributions (a) at 0.36 THz for *y*-polarized incident wave and (b) at 0.71 THz for *x*-polarized incident light before the VO_2 phase transition. The simulated electric field distributions (c) at 0.40 THz for *y*-polarized incident wave and (d) at 0.87 THz for *x*-polarized incident light after the VO_2 phase transition.

transition at 300 K, the ellipticity at 0.45 THz is 0.998, and at 1.10 THz, the ellipticity is –0.971. This indicates that at 0.45 THz, the output THz is a left-handed circularly polarized light, while at 1.10 THz, the output THz is a right-handed circularly polarized light. After the VO_2 phase transition, the operating frequencies are switched to 0.50 and 1.05 THz with the corresponding ellipticity of 0.999 and –0.999. Therefore, at these four operating frequencies, the phase-change metasurfaces present a high degree of linear-to-circular polarization conversion. The numerical simulation shown in Fig. 4(b) indicates similar results with the experiment.

To further elucidate the working mechanism of this phase-change metasurface, the electric field distributions of the C-ESRRs at different resonance frequencies are simulated to analyze the resonance modes and their interactions. In principle, when two resonators are orthogonal to each other with a slight difference in the resonance frequencies, there would be an overlapping region in between where the resonance intensities are the same, but the phases are relatively retarded. By precisely controlling the resonances, one can achieve the same resonance intensity with 90° phase retardance at a certain frequency. Fig. 5(a) and (b) present the electric field distributions before the VO_2 phase transition at 0.36 and 0.71 THz with respect to *y*- and *x*-axes polarized incident light, respectively. It is observed that the resonance at 0.36 THz corresponds to the LC resonance of C-ESRRs. The resonance at 0.71 THz corresponds to the dipole resonance of C-ESRRs. These two resonance modes are perpendicular to each other with a frequency difference. The overlapped area at 0.45 THz presents around 90° phase delay, making the device work as a quarter-wave plate. A similar overlapping area can be observed at 1.10 THz with around 90° phase delay. Thus, the quarter-wave plate presents two operating frequencies at 0.45 and 1.10 THz. After the VO_2 phase transition, the electric field distributions at 0.40 and 0.87 THz are shown in Fig. 5(c) and (d). It is observed that the inserted VO_2 changes the effective length of the resonators. Both the LC resonance and dipolar resonance are shifted, making the operating frequencies of the quarter-wave plate shift to 0.50 and 1.05 THz. In our design, the VO_2 pads are not fully covered with the gap in the C-ESRRs. This is necessary to design two operating frequencies. If the VO_2 pads fully cover the gap, the LC resonance would be switched off, instead of shifting to a different frequency when VO_2 goes through the semiconductor to metal phase transition.

4. Conclusion

In summary, we have designed and experimentally demonstrated a multiband switchable THz quarter-wave plate via phase-change metasurfaces. The phase-change metasurfaces are composed of complementary electric split-resonators embedded with vanadium dioxide. In the experiment, we achieved linear-to-circular polarization conversion at 0.45 and 1.10 THz with an ellipticity of 0.998 and −0.971 before the VO_2 phase transition. After the VO_2 phase transition, linear-to-circular polarization conversion was obtained at 0.50 and 1.05 THz with an ellipticity of 0.999 and −0.999, respectively. The simulated electric field distributions indicate that the inserted VO_2 pads change the effective length of the resonators and lead to this multiband switching. This multiband active phase-change metasurface reveals a new avenue for multiband THz ultrathin meta-device design and can be extended to make other polarization manipulation devices.

References

[1] A. V. Kildishev, A. Boltasseva, and V. M. Shalaev, "Planar photonics with metasurfaces," *Science*, vol. 339, no. 6125, Mar. 2013, Art. ID 1232009.

[2] N. I. Zheludev and Y. S. Kivshar, "From metamaterials to metadevices," *Nat. Mater.*, vol. 11, no. 11, pp. 917–924, Nov. 2012.

[3] N. K. Grady *et al.*, "Terahertz metamaterials for linear polarization conversion and anomalous refraction," *Science*, vol. 340, no. 6138, pp. 1304–1307, Jun. 2013.

[4] Y. Zhao and A. Alu, "Manipulating light polarization with ultrathin plasmonic metasurfaces," *Phys. Rev. B, Condens. Matter Mater. Phys.*, vol. 84, no. 20, Nov. 2011, Art. ID 205428.

[5] D. C. Wang, C. W. Qiu, and M. H. Hong, "Coupling effect of spiral-shaped terahertz metamaterials for tunable electromagnetic response," *Appl. Phys. A*, vol. 115, no. 1, pp. 25–29, Apr. 2014.

[6] M. B. Pu *et al.*, "Broadband anomalous reflection based on gradient low-Q meta-surface," *AIP Adv.*, vol. 3, no. 5, May 2013, Art. ID 052136.

[7] D. C. Wang, Q. Huang, C. W. Qiu, and M. H. Hong, "Selective excitation of resonances in gammadion metamaterials for terahertz wave manipulation," *Sci. China, Phys. Mech. Astron.*, vol. 58, no. 8, Aug. 2015, Art. ID 084201.

[8] M. Pu *et al.*, "Catenary optics for achromatic generation of perfect optical angular momentum," *Sci. Adv.*, vol. 1, no. 9, Oct. 2015, Art. ID e1500396.

[9] N. F. Yu and F. Capasso, "Flat optics with designer metasurfaces," *Nat. Mater.*, vol. 13, no. 2, pp. 139–150, Feb. 2014.

[10] X. G. Luo, "Principles of electromagnetic waves in metasurfaces," *Sci. China, Phys. Mech. Astron.*, vol. 58, no. 9, Sep. 2015, Art. ID 09421.

[11] W. T. Chen *et al.*, "High-efficiency broadband meta-hologram with polarization-controlled dual images," *Nano Lett.*, vol. 14, no. 1, pp. 225–230, Jan. 2014.

[12] A. C. Strikwerda *et al.*, "Comparison of birefringent electric split-ring resonator and meanderline structures as quarter-wave plates at terahertz frequencies," *Opt. Exp.*, vol. 17, no. 1, pp. 136–149, Jan. 2009.

[13] N. F. Yu *et al.*, "Light propagation with phase discontinuities: Generalized laws of reflection and refraction," *Science*, vol. 334, no. 6054, pp. 333–337, Oct. 2011.

[14] F. Qin *et al.*, "Hybrid bilayer plasmonic metasurface efficiently manipulates visible light," *Sci. Adv.*, vol. 2, no. 1, Jan. 2016, Art. ID e1501168.

[15] P. Genevet *et al.*, "Ultra-thin plasmonic optical vortex plate based on phase discontinuities," *Appl. Phys. Lett.*, vol. 100, no. 1, Jan. 2012, Art. ID 013101.

[16] G. X. Zheng *et al.*, "Metasurface holograms reaching 80% efficiency," *Nat. Nanotechnol.*, vol. 10, no. 4, pp. 308–312, Apr. 2015.

[17] X. Q. Su *et al.*, "Broadband terahertz transparency in a switchable metasurface," *IEEE Photonics J.*, vol. 7, no. 1, Feb. 2015, Art. ID 5900108.

[18] X. Su *et al.*, "Active metasurface terahertz deflector with phase discontinuities," *Opt. Exp.*, vol. 23, no. 21, pp. 27152–27158, Oct. 2015.

[19] D. C. Wang *et al.*, "Switchable ultrathin quarter-wave plate in terahertz using active phase-change metasurface," *Sci. Rep.*, vol. 5, Oct. 2015, Art. ID 15020.

[20] H. Cheng *et al.*, "Dynamically tunable broadband infrared anomalous refraction based on graphene metasurfaces," *Adv. Opt. Mater.*, vol. 3, no. 12, pp. 1744–1749, Dec. 2015.

[21] O. Buchnev, N. Podoliak, M. Kaczmarek, N. I. Zheludev, and V. A. Fedotov, "Electrically controlled nanostructured metasurface loaded with liquid crystal: Toward multifunctional photonic switch," *Adv. Opt. Mater.*, vol. 3, no. 5, pp. 674–679, May 2015.

[22] S. K. Earl *et al.*, "Tunable optical antennas enabled by the phase transition in vanadium dioxide," *Opt. Exp.*, vol. 21, no. 22, pp. 27503–27508, Nov. 2013.

[23] T. J. Cui, M. Q. Qi, X. Wan, J. Zhao, and Q. Cheng, "Coding metamaterials, digital metamaterials and programmable metamaterials," *Light, Sci. Appl.*, vol. 3, no. 10, p. e218, Oct. 2014.

[24] L. H. Gao *et al.*, "Broadband diffusion of terahertz waves by multi-bit coding metasurfaces," *Light, Sci. Appl.*, vol. 4, no. 9, p. e324, Sep. 2015.

[25] S. Zhang *et al.*, "Photoinduced handedness switching in terahertz chiral metamolecules," *Nat. Commun.*, vol. 3, no. 7, p. 942, Jul. 2012.
[26] D. C. Wang, Y. H. Gu, Y. D. Gong, C. W. Qiu, and M. H. Hong, "An ultrathin terahertz quarter-wave plate using planar babinet-inverted metasurface," *Opt. Exp.*, vol. 23, no. 9, pp. 11114–11122, May 2015.
[27] Z. C. Chen, Y. D. Gong, H. Dong, T. Notake, and H. Minamide, "Terahertz achromatic quarter wave plate: Design, fabrication, and characterization," *Opt. Commun.*, vol. 311, pp. 1–5, Jan. 2014.
[28] L. Q. Cong *et al.*, "Highly flexible broadband terahertz metamaterial quarter-wave plate," *Laser Photon. Rev.*, vol. 8, no. 4, pp. 626–632, Jul. 2014.